Journal of Applied Geophysics 188 (2021) 104307

Contents lists available at ScienceDirect

Journal of Applied Geophysics

journal homepage: www.elsevier.com/locate/jappgeo

Geological and geophysical investigations of an engineering site characterization for construction purposes in Western Saudi Arabia

Paul Irikefe Edigbue [a], Abdullah Abobakr Al-Mashhor [a], Anastasios Plougarlis [b], Pantelis Soupios [a,*], Markos Tranos [a], SanLinn Kaka [a], Abdullatif Al-Shuhail [a], Mansour Al-Garni [c]

[a] Geosciences Department, King Fahd University of Petroleum & Minerals, Dhahran, Saudi Arabia
[b] School of Geology, Aristotle University of Thessaloniki, Greece
[c] Department of Geophysics, King Abdulaziz University, Jeddah, Saudi Arabia

ARTICLE INFO

Article history:
Received 23 July 2020
Received in revised form 5 March 2021
Accepted 8 March 2021
Available online 14 March 2021

Keywords:
Electrical resistivity tomography survey
Site characterization
Geological mapping
Transient electromagnetic survey
Geothermal fluids

ABSTRACT

Characterizing subsurface site conditions and understanding main geological features are critical components of any safety assessment for any construction, particularly defining subsurface flow paths and weakness (i.e. fracture and fault) zones. Poor definition of flow paths and weakness zones may lead to serious hazards during construction. This study, integrating geophysical and geological investigations, is undertaken to enhance the understanding of both surface and subsurface complexities of an engineering site characterization located in western Saudi Arabia near Red Sea. Two geophysical investigations, Electrical Resistivity Tomography (ERT) and Transient Electromagnetic (TEM), were carried out to characterize the subsurface of the study area. A total of three ERT profiles and sixteen TEM sounding measurements was conducted in the study area. Geological investigation was mainly focused to understanding geological features and bedrock conditions of the two opposite river's abutments at the study site. Geophysical results show NNE-SSW and NNW-SSE fault zones which were confirmed by in-situ geological inspections and by satellite images. The results also reveal the presence of geothermal fluids validated by the observation of hot water flowing in the river along the measurements. This study demonstrates that the integrated geophysical and geological investigations provide means to infer geothermal fluids, locate fractures, and fault zones. This study enabled us to characterize and locate the geological structural framework as well as possible geothermal fluids existence in the study area.

1. Introduction

Site characterization is an important step in civil engineering study or design. In order to devise a design for an engineering project such as urban development, a range of conceptual factors need to be assessed. An important factor that should be taken into account is the geological situation at the site. Therefore, a geological assessment should be implemented prior to any constructions. A proposed site in the western part of Saudi Arabia, near the Red Sea (Fig. 1), was planned by the government to be developed. For that reason, the subsurface characterization of the local geological and tectonic conditions (Fig. 2) were needed and a geophysical survey was suggested. Thus, detailed geological and geophysical studies were carried out to conduct full assessment of the under-development site. Geophysical survey at the study area suggests that the site has been affected by almost *E*-W fault system that resulted in two depressions (Al-Homoud et al., 1995), which extended in the form of buried structural channels filled with porous alluvium and fractured greenstone rocks (Moustafa et al., 2013). These depressions are considered permeable zones and represent a favorable pathway for groundwater flow. Consequently, further geological and geophysical surveys are necessary to better characterize the site (Wang et al., 2019). Therefore, we carried out detailed geological and geophysical investigations to define the tectonic geological features, such as the existence of main faults, and to better understand the subsurface geological conditions. Detailed geological studies have been conducted at the exposed rocks of the two abutments of the site in order to identify rock types as well as the delineation of the tectonic features, especially those related to faulting at the proposed site. Geophysical survey has been conducted using electrical resistivity tomography (ERT) and transient electromagnetic (TEM) methods to characterize the subsurface geological elements such as geological structures and identify different subsurface fault zones.

2. Geological setting

Wadi Al-Lith, originating from the east of the Oarnayt Mountains in the south of the city of Taif, drifts to the South, enhanced by the water of

* Corresponding author.
E-mail address: panteleimon.soupios@kfupm.edu.sa (P. Soupios).

https://doi.org/10.1016/j.jappgeo.2021.104307
0926-9851/

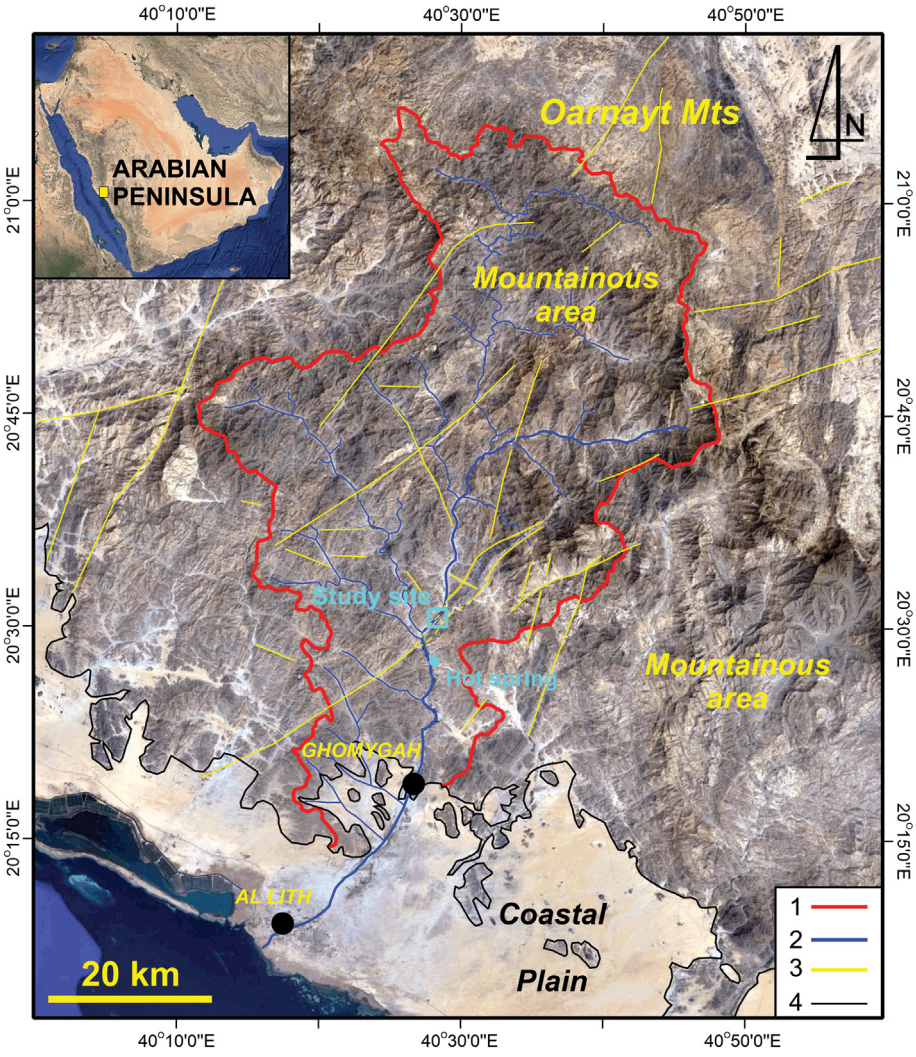

Fig. 1. Satellite Google Earth image of the catchment area of the study site. Explanation: 1. Watershed, 2. Hydrographic network, 3. Main lineaments as derived from analysis of satellite images, 4. Coastal plain-bedrock contact.

several tributaries, and finally discharges into the Red Sea through the city of Al-Lith (Fig. 1). Most part of the hydrographic network of Wadi Al-Lith is developed on the Precambrian crystalline rocks of the Arabian Shield forming the low, but rugged mountainous area, and only the last 27 km of the stream beds (i.e., south of Ghomygah town) run through the coastal plain (Fig. 1). The latter is filled up with Quaternary deposits such as alluvium, pediment and plain sand, gravel, and silt and aeolian dune fields (Hadley and Fleck, 1979; Al-Sanad et al., 1993). The geology of the Al-Lith region was first mapped at a scale of 1:500.000 (Brown et al., 1963). Since then, little geologic work has been conducted in the area, including the geological mapping at a scale of 1:100.000 (Wier and Hadley, 1975; Hadley and Fleck, 1980). According to this geological mapping, the area is covered by Precambrian layered and intrusive rocks consisting of two volcanic sequences, the Baish and Jiddah Groups, which are metamorphosed to the greenschist facies. In particular, the volcanic flow rocks of basaltic to rhyolitic compositions and associated stratified volcaniclastic rocks are grouped into Baish Group, whereas the andesite flow rocks are grouped into the Jiddah Group (Hadley and Fleck, 1980). Basalt samples were dated using Rb-Sr radiometric techniques yield an age of 1165 ± 110 m.y., with an $87Sr/86Sr$ initial ratio of 0.70289 ± 0.00003 (Fleck et al., 1980). Along with these volcanic sequences, a wide variety of intrusive rocks ranging in composition from gabbro and diorite to granite build up the mountainous terrain through which the Wadi Al-Lith drifts to the Red Sea. The rocks of the Baish and Jiddah Groups trend from NS to NE-SW and dip at vertical to near-vertical angles. They are tightly folded in several places with fold axes and lineation following the same NS to NE-SW trend. The youngest magmatic activity in the region is recorded by the Miocene gabbro dikes, which have been dated to be about 22 m.y. old (Brown, 1970; Coleman et al., 1972). It is related to the extension and the tectonic events associated with an initial opening of the Red Sea (Coleman, n.d.; Coleman and Donato, 1979), and the late Miocene and Pliocene uplift of the Red Sea escarpment (Ross and Schlee, 1973) due to faulting, as the latter implied by the tilting of the youngest boulder conglomerates of the Bathan Formation towards NE at 15° during the Pliocene. Note that in and around Wadi Al-Lith, characteristic is the presence of hot springs (Fig. 1) with surface temperatures varying from 41 to 96 °C (Lashin et al., 2014). According to these authors, these hot springs manifest the existence of a geothermal field in the area. These hot springs are located approximately 5Km South of the study area, have been reported since 1975 (Wier and Hadley, 1975), and are vital for further urban development.

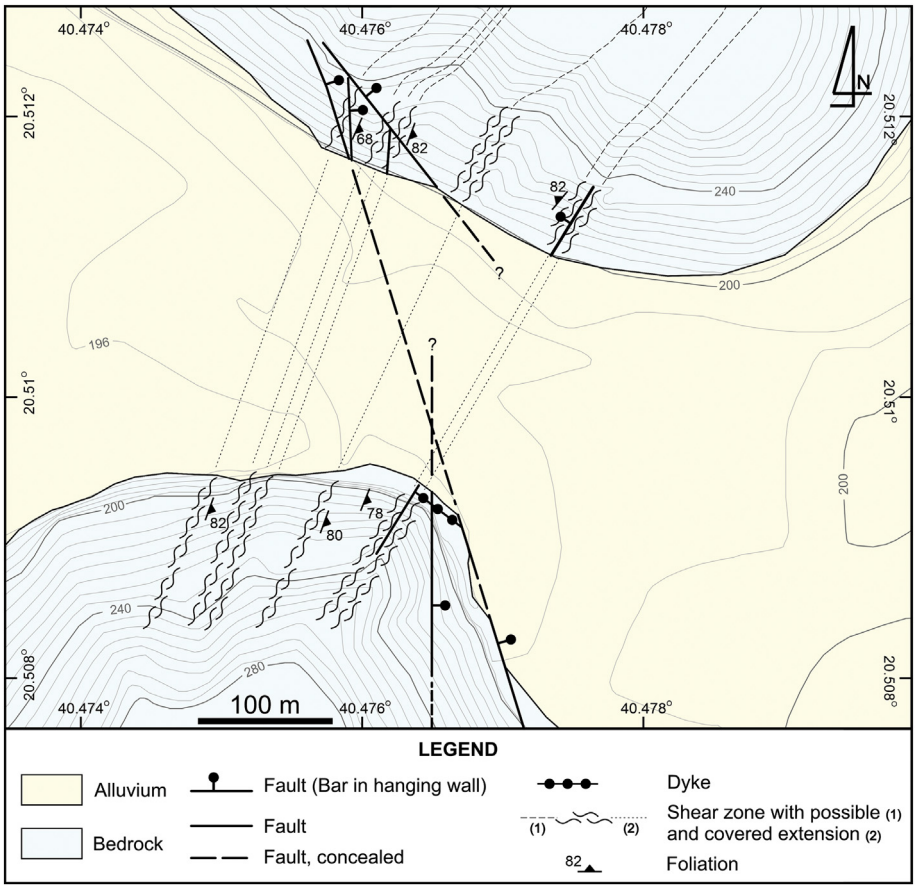

Fig. 2. Tectonic geological map of the study area. Contours indicate elevation from mean sea level (NESPAK – National Engineering Services Limited Pakistan, 2014).

3. Geological investigation - Geology of the study site

The study site has been chosen just downstream of a distinct right meandering curve (Fig. 1). The interpretation of Landsat RGB images with resolution of 30 m and images as provided by Google Earth shows that the fracture pattern in the region is dominated by 1st order and 2nd order photo-lineaments. The first correspond to NNE- to NE-trending km-long shear to fault zones, and the second to NW- to WNW-trending discontinuous fractures or faults. Both of them dominate the basement rocks controlling at places the hydrographic network giving rise to bends or meandering curves along the stream drift to the south (Fig. 1). The study site is along a such bend making its geological setting much more complicated. (Wier and Hadley, 1975; Hadley and Fleck, 1980) suggest numerous such steeply dipping to vertical faults stating that these faults could not be recognized in the field since they do not cause any apparent displacement to the drainage pattern. In many places (Hadley and Fleck, 1980) mapped NW-SE trending dikes, i.e., parallel to such faults, and assigned them as Miocene gabbro dikes. At the study site (Fig. 2), the valley is filled by alluvial deposits like sands and gravely sands, whereas the water flows by the northern abutment. It is worth noting that while we are conducting the geophysical survey, hot water was intensely sensed to the left bank of the current stream and at distance of about 180 m from the left abutment. The exposed rocks on the study site, and particularly on the right and left abutments, are greenstones and greenschists metamorphosed from basalts, andesites and volcaniclastic rocks. In general, they are strongly sheared and trending NNE-SSW with a series of anastomosing semi-brittle shear zones and have been metamorphosed to the greenschist facies. Bedding can scarcely be recognized, but where this was possible, beds were generally 5–10 cm thick. Our field work at the study site was mainly focused on the inspection of the two opposite abutments, trying to define the main geologic structures and features of the exposed rocks. The description of these abutments is as follows, where the attitude of the structures is given with dip direction and dip angle (dipD/dipA):

3.1. Left abutment (E-W trend)

In this abutment, the exposed rocks are greenstones and greenschists originated from mafic igneous rocks. The greenschists are less competent, strongly foliated and stretched, because the original rocks are more volcaniclastic rocks than lava flows. Two subvertical foliations, S1 and S2, have been recognized (Fig. 3a) striking NE-SW and NNE-SSW, respectively. The S1 seems to be parallel to bedding (S0), whereas S2 is the dominant foliation of the rocks. The latter occurs as a mylonite foliation along the similarly trending semi-brittle shear zones (Fig. 2), but also as crenulation or spaced schistosity to difficulty seen mesoscale folds. The greenstones are massive, and because of this, brittle structures are easily observed (Fig. 4). A large normal fault zone (Figs. 2, 3a, and 4) striking NNW-SSE has been found at the eastern edge of the abutment with high angles, whereas dense steeply-dipping to sub-vertical fractures similarly striking NNW can be considered as part of the damage fault zone. Also, at the center of the greenstone exposure, an N-S striking fault (Figs. 2, 3a, and 4) has been recognized to affect the NNW-SSE striking fracture zones, but also small vertical to sub-vertical Qz-extension veins. These Qz-extension veins striking about N110°, have length commonly less than 0.3 m (rarely less than 1 m) and width of few cm. In addition, the rocks are intruded by a

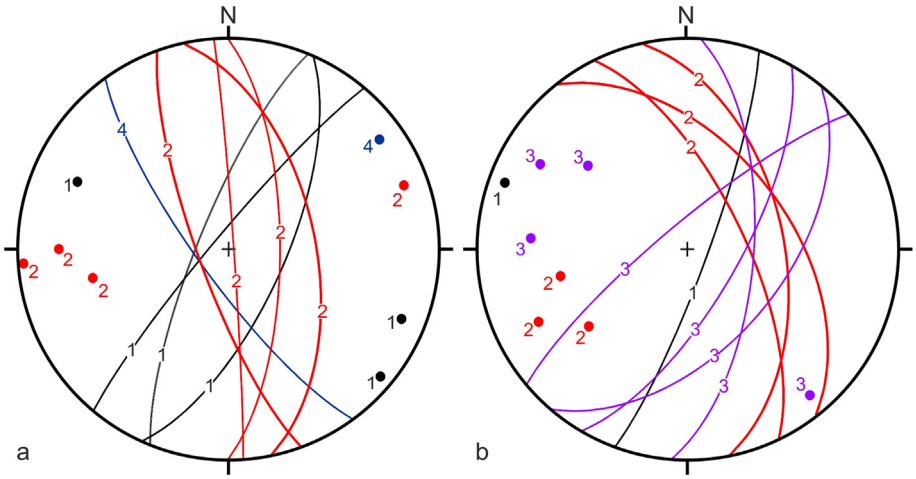

Fig. 3. Equal area, lower hemisphere projection of the main structural elements of the (a) Left and (b) right abutment. Explanation: 1 = foliation, 2 = faults, 3 = shear to fault zones, 4 = dyke.

mafic dyke with width ranging from 1.5 to 2 m, which dips steeply towards SW (Figs. 2, 3a, and 4), as the gabbro dikes that have been mapped by (Wier and Hadley, 1975; Hadley and Fleck, 1980). (See Fig. 5.)

3.2. Right abutment (WNW-ESE trend)

The right abutment has a WNW-ESE trend and the exposed rocks are alternations of greenstones and greenschists, while some interlayers of sericite schists occur. The main foliation (S2) strikes NNE-SSW and dips steeply towards ENE or is almost vertical (Figs. 2 and 3b). A N-S striking narrow vertical semi-brittle shear to fault zone of width no more than 0.5 m and strike-slip sense-of-shear occur at the westernmost part of the abutment (Figs. 2 and 3b) and it is cut by NW-NNW extensional faults (Fig. 2). The latter dip towards NE-ENE at medium- to steep angles and show normal and oblique normal displacements (Fig. 1). At the eastern side of the abutment, a NE-SW striking strike-slip semi-brittle shear to fault zone with attitude, and width of 2 m occurs (Fig. 2).

4. Geophysical survey

Among all geophysical methods, resistivity and electromagnetic methods considered to be the leading ones in the exploration of groundwater (Li et al., 2020; Sudha et al., 2011; Rahimi et al., 2018; Smith and Randazzo, 1986; Loperte et al., 2016). Many successful applications of these methods reported in the literature have to do with seawater intrusion detection and monitoring and fracture zone identification. Both methods are sensitive to the same physical property, electrical conductivity, but they feel it differently. The DC method has a longer history (since 1912) than EM methods and it has a wide range of applications to environmental and engineering problems. Electrical measurements are more sensitive to resistive contrasts whereas, TEM method does not work properly in high resistive region. TEM method is a fast and cost-effective method and can provide deeper penetration depth capability and greater resolving power (Everett and Meju, 2005) but at the same time, it is sensitive to cultural noise sources, such as power lines, pipelines, etc., that decrease the signal-to noise ratio. Both methods were carried out on the stream bed of the study site, at about 200 m mean sea level, aiming to delineate the possible structures, determine the bedrock depth, describe the vertical and lateral resistivity variations as well as any significant features related to geothermal fluids (Smith and Randazzo, 1986).

Geophysical (ERT and Seismic refractions) surveys were conducted at the study area and used to evaluate the recent geophysical findings. Specifically, three seismic lines were conducted (Fig. 6, yellow lines, A-A', B-B′ and C-C′), and showed that the site is affected by faulting that

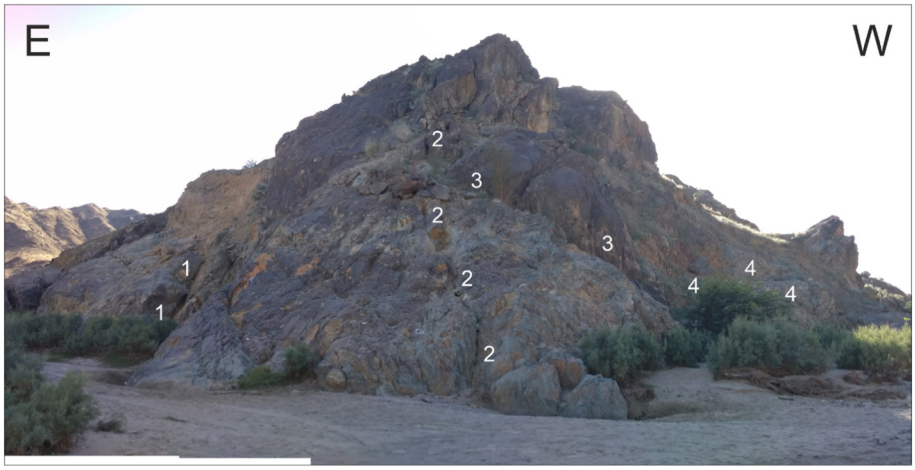

Fig. 4. General view of the left abutment of the study site. (1), (2) Faults, (3) Dyke, (4) semi-brittle shear to fault zones.

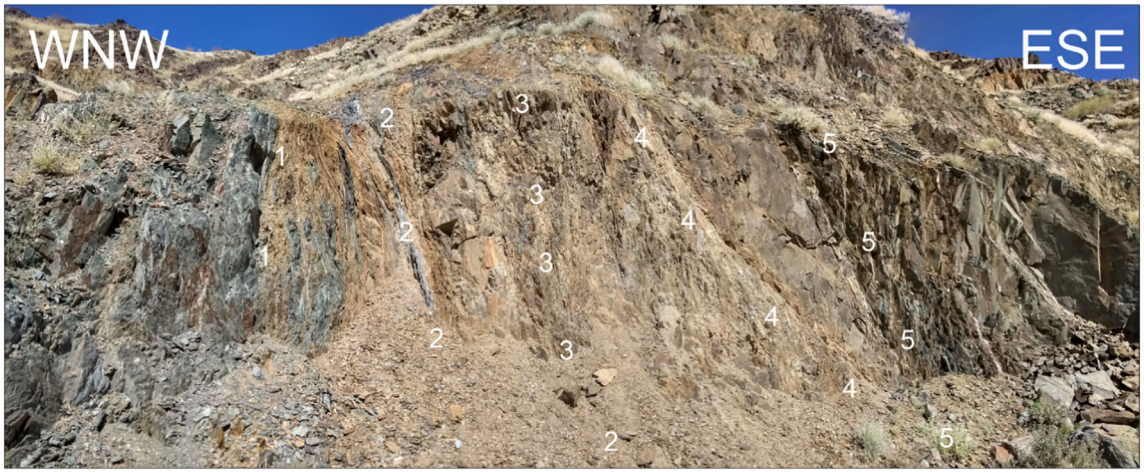

Fig. 5. An array of NNE-SSW trending heterogeneous and anastomosing semi-brittle shear zones to fault zones (1, 2, 3, 4, and 5) at the right abutment of the study site.

formed two depressions. These depressions included, buried channels filled with porous alluvium and/or fractured bedrock which acted as preferable pathways (high with permeability) for groundwater flow. This conceptual model was confirmed as a low resistivity zone of thickness up to 22 m, by an ERT profile along the A-A' section conducted in this study. The location of the water seepage and the beginning and end of the previous (3 seismic and an ERT profiles) geophysical surveys were georeferenced and used for confirmation/comparison of the current geophysical survey.

The current geophysical work comprises of three ERT profiles and sixteen TEM sounding measurements (Fig. 2). The distribution of the ERT profiles and TEM soundings was strongly controlled by the current water flow and the location of the safeguard barrier within the study area. Topographic correction was not necessary as the survey area is flat.

Based on preliminary results of ERTs and the geometry of the study area, TEM soundings were carried out at locations where ERT lines were not accessible. TEM soundings cover north and northwest part of the study area. The location of the electrodes along the ERT profiles

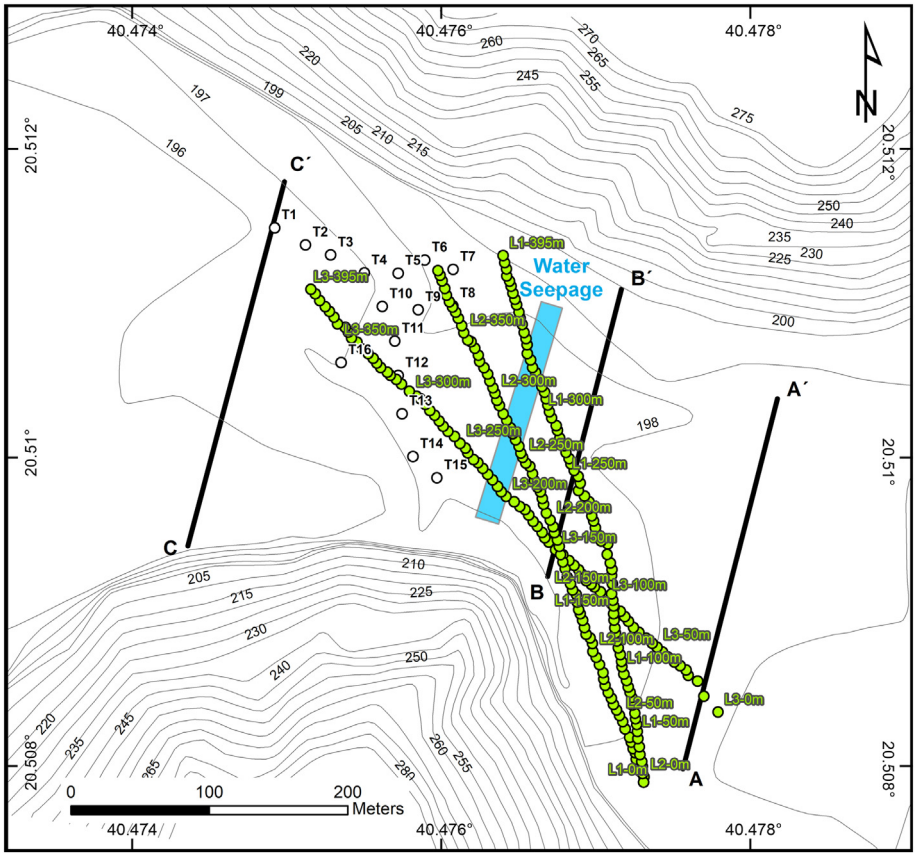

Fig. 6. The locations of three ERT profiles (green squares represent the electrodes' location and the offset from the begging in meters) from South to North and TEM soundings (as circles, T #) are shown. The location of three refraction seismic profiles (A-A', B-B′ and C-C′) acquired by (Moustafa et al., 2013) are shown as yellow lines and the water seepage area are shown as blue shaded rectangle) as defined by (NESPAK – National Engineering Services Limited Pakistan, 2014).

and the TEM soundings were determined using the Garmin 60CSx GPS unit.

4.1. Electrical resistivity tomography

Three ERT profiles of 395 m total length, were acquired using 80 electrodes with 5 m electrode spacing, achieving accuracy of 2.5 m in vertical, and 5 m lateral resolution. The SYSCAL Pro 96 resistivity meter was used to acquire the data, whereas the inversion was performed using RES2DINV software (Loke, 2004). A finite-difference grid with 2 nodes between adjacent electrodes and proper regularization parameters during the inversion process were applied. Different acquisition configurations, (Dipole-Dipole-DD and Wenner-Schlumberger-WS), were chosen to achieve the highest lateral (DD) and vertical (WS) resolutions of the final reconstructed geophysical models (Simyrdanis et al., 2018; Demirci et al., 2017; Ntarlagiannis et al., 2016; Moisidi et al., 2013). Based on the number of data's layers (n) and the acquisition configurations, the final tomographic models reached the maximum depth of 87 m. The DD and WS data were processed separately and were later combined (DD + WS) to invert the unified data file. The average misfit of the final inverted geoelectrical models was less than 6.5%.

4.2. Transient electromagnetic method

Based on the principles of electromagnetism, secondary currents can be induced in the subsurface by a time-varying electromagnetic field. The secondary magnetic fields generated by the secondary currents can then be measured by appropriate electromagnetic receivers (Nabighian, 1988). Transient electromagnetic method (TEM) (Rani et al., 2020; Kalisperi et al., 2018; Autio et al., 2016; Kanta et al., 2013; Soupios et al., 2010) measures the decay of the amplitude as a function of time on a transient wave. The decay time is proportional to the resistivity change in the ground (Nabighian, 1988; Kirsch, 2006; Everett, 2013; Reynolds, 2011). TEM method creates a magnetic field by passing an electrical current through a transmitter loop. When the current is cut off the change in magnetic field induces a current (known as eddy current) in the subsurface according to Maxwell's equations. This system of eddy currents produces a secondary magnetic field. The secondary magnetic (B) field (due to subsurface inhomogeneity) induces current in the receiver loop (coil) and the acquisition system records the electrical potentials. The temporal variation of the secondary magnetic field (dB/dt) can be transformed to apparent resistivity, which depends on the subsurface properties (Nabighian, 1988; Everett, 2013; Hoekstra and Blohm, n.d.). Sixteen TEM soundings were acquired in the study area. The ABEM- WalkTEM system by ABEM was used to acquire the data. A central square loop configuration with a single-turn (40 m side, loop area 1600 m2) was utilized as a transmitter loop whereas one coil (0.5 m side square loop with 20 internally turns in the center of the transmitter loop, giving a total receiving area of $5m^2$) was used to receive the signal. To increase the signal to noise ratio (S/N), three cycles of measurements over the same location were stacked. A battery of 12 V was used to power the whole system with an average input current of 6.2A. The dual (low and high) moment 25 ms (milliseconds) with 45 gates acquisition protocol was used. The total measuring time, 24.538 ms (or 24,538μs) is divided into 45 time-gates to collect shallow and deep data. The shortest gate is 2μs and the longest gate is 4765μs. The low moment is used for early-time gate measurements (near-surface mapping), whereas the high moment is applied for later-time gate measurements (characterization of the deeper layers). The Aarhus SPIA was used for processing (filtering and inversion) of TEM data (Fig. 7). The Aarhus Workbench software (Denmark Skolegade 21, 2020) was used for the visualization of the results. A quasi-2D resistivity section was finally generated to show the resistivity range with depth along with the TEM profile. The average misfit of the final inverted TEM soundings was 2.8%.

5. Geophysical results

5.1. ERT results

The first ERT profile (L1) acquired using the dipole-dipole configuration and the final tomographic resistivity section are shown in Fig. 8. Note that the description of the ERT profiles and the relative distances are given from their beginning, which is to the south. The bedrock, with resistivity higher than 400 Ohm.m, was found at a depth of 10 m, from the beginning (South) of the profile at 190 m offset, along the ground surface. After 190 m offset, a sudden lateral disrupt of the high resistivity formation (bedrock) which is possibly related to a geological lateral discontinuity is depicted as Anomaly A in Fig. 8. The same geoelectrical basement (bedrock) is detected after 230 m offset from the beginning of the profile at the depth of 70 m. However, it is risky to make such an assumption since the high resistivity anomaly was found at the edge of the model (edge effects) where the uncertainty in the interpretation is the highest (see question mark at that location). At shallow depth, (in the upper 15 m) very low resistivity zone (5–15 Ohm.m) (Fig. 8, anomaly B) was detected at the end (from 320 to 395 m) of the profile. The RMS errors of the L1 was 2.9% after five iterations. The second profile (L2) was subparallel (towards to SSE-NNW) to L1 and was acquired using the dipole-dipole configuration. The final inverted resistivity model for L2 show similarity to L1 in terms of structural characteristics. The bedrock (surrounded by a dotted white line) was found at a depth of 10 m, from the beginning (South) of the profile until the 185 m offset, along the ground surface. Then, there is a lateral discontinuity (anomaly A) with relatively medium resistivities varying from 100 to 300 Ohm.m. The bedrock was detected after 240 m offset from the beginning of the profile at a depth of 70 m (at the question mark), but as mentioned above, it is risky to make any safe assumption since this high resistivity anomaly was found at the edge of the model due to possible edge effects. This lateral resistivity discontinuity can be interpreted as a structural/geological discontinuity. A shallow very low resistivity zone (5–20 Ohm.m), covering the upper 20 m of the resistivity cross section (Fig. 8, anomaly B), was detected close to the end (from 320 to 395 m) of the profile as in L1. The RMS errors of L2 was 6.8% after four iterations. The L3 ERT profile was acquired from SE to NW and crossed the other two (L1 and L2) profiles. The same number of electrodes (80), layers and electrode's spacing was used as the previous profiles. The only difference was on the geometrical configuration used in the acquisition which was a combination of dipole-dipole and Wenner-Schlumberger (achieving the highest lateral and vertical resolution). As mentioned, L1 and L2 failed to penetrate deeper and provide a clear image of the bedrock after 240 m along the profile (where the question mark is placed). Thus, by using the WS configuration, we were able to confirm our assumption about the appearance of the bedrock at about 70 m depth and to infer some geometrical characteristics of this anomaly zone (anomaly A in Fig. 8). All three ERT resistivity sections using the different acquisition configurations (from DD, WS and combined DD + WS) are presented in Fig. 8. Both configurations have resulted in similar tomographic images were the bedrock detected at the same depth (at around 70 m) and horizontal location. However, by applying the WS configuration (as mentioned above), we were able to reach the maximum depth of 87 m and confirm the lower block of the bedrock. Similar results were obtained from the joint interpretation of the WS and DD, as shown below. Based on WS resistivity section, the disruption zone has apparent (depending on the real orientation of this zone) width (gap) of about 30 m and a bedrock throw of about 56 m, as is shown in Fig. 8. In L3, the shallow low resistivity zone (anomaly B) is much more limited and sparser than in L1 and L2 and found between 240 and 330 m along the L3. The RMS errors of the L3-DD, L3-WS and L3-DD + WS was 13.2%, 3.4% and 13.6% after five, four and five iterations, respectively. In summary, in all ERT profiles (L1, L2 and L3), the

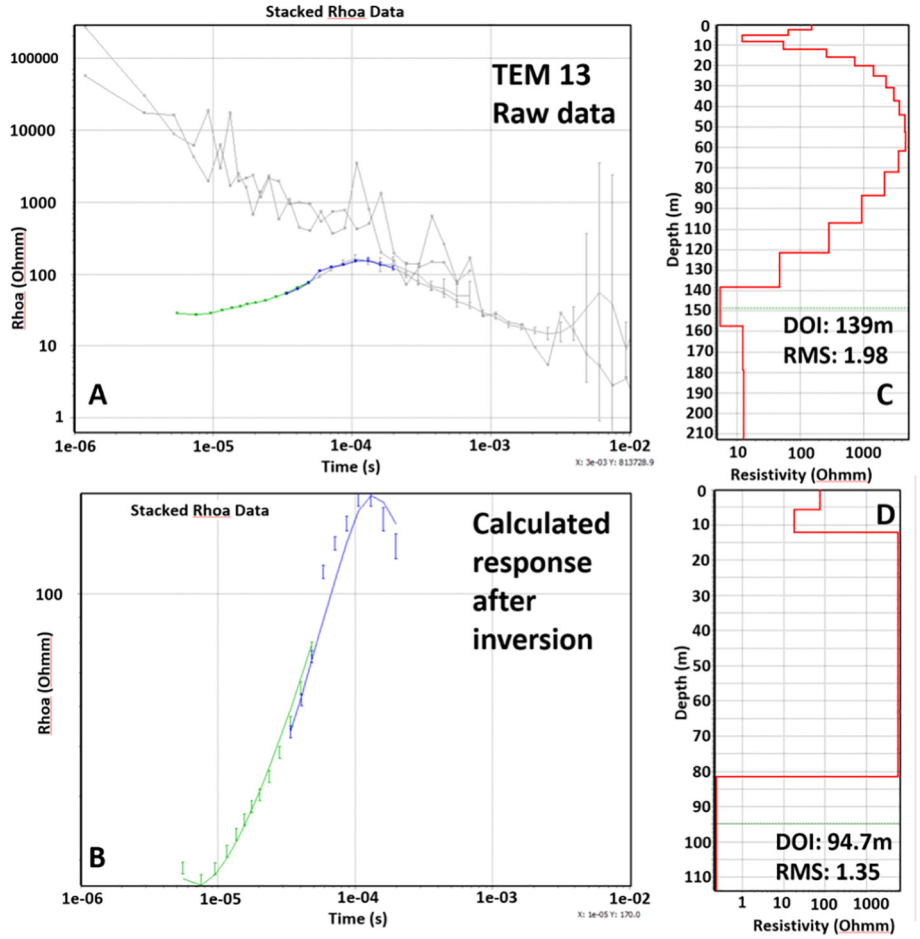

Fig. 7. The raw (A), processed (B) and final resulted smoothed (C) and layered (D) inverted model for TEM 13 site are shown. The DOI (depth of investigation) and RMS errors are also shown for each resistivity model.

stratigraphy of two geological layers is the profound feature for almost their southern half parts, whereas much more complicated structure characterized the northern half part of the profiles, where this stratigraphy can hardly be seen. The two-layer stratigraphy consists of the uppermost layer that has resistivities varying from 20 to 80 Ohm.m (corresponding to saturated alluvium) and resistivities from 400 to 700 Ohm.m (corresponding to unsaturated/compacted alluvium composed of gravels, pebbles and sand detected at the end of the third profile). The underlying layer with resistivity higher than 700 Ohm.m corresponds to the bedrock found in the study area. In the northern half part of the profiles, only the first layer (alluvium) dominates. In particular, close to the northern end of the profiles, very low resistivity (5–20 Ohm.m) anomaly has also been recognized as the most surficial layer (on L1 and L2) with abnormal base boundary in L3. The ERT results agreed well with the velocity model as obtained from the interpretation of the B-B′ section from (Moustafa et al., 2013). Fig. 9 shows that ERT (L3, L2 and L1) profiles crossed B-B′ refraction profile at 11 m, 28 m and 81 m, respectively. The estimated depth to bedrock (at about 72 m below ground surface) from the seismic data, fit well with the depth of the high resistivity zone found (at 70 m below ground surface) in the study area along all three profiles.

5.2. Transient electro magnetic – TEM

A total of sixteen sounding measurements has been used to generate the resistivity section. Thus, a quasi-2D resistivity section is constructed from the interpolation of the smoothed final resistivity models using the Aarhus Workbench (AGS Aarhus Geosoftware 2020) and presented in Fig. 10. The resistivity section is represented by four layers model, characterizing the spatial and vertical resistivity variations along the NW-SE trending TEM profile as seen in Fig. 10. The first layer is characterized by very low resistivity values (less than 20 Ohm.m, dark blue color) where this layer has been detected by all three ERT profiles (close to the end of its profile). Furthermore, this layer was also observed by the field crew where they experienced spots of hot water within the river during the setup and acquisition of ERT measurements. The second layer exhibits resistivity variations ranging from 20 to 90 Ohm.m (light blue color). The third layer is characterized by a relatively higher resistivity values (90–250 Ohm.m, green color) whereas the deeper geoelectric layer (fourth layer) is characterized by even higher resistivity values reaching more than 250 Ohm.m. The very low resistivity zone seems to be mainly extended to the South (Fig. 10).

6. Discussion-interpretation

The study site is dominated by both massive fractured greenstones derived from the basaltic and andesitic lava flows and more friable greenschists, which have been subjected to intensive foliation and shearing, derived from volcaniclastic rocks of the same composition. The foliation of the exposed rocks and the contacts between them strike NNE-SSW and dip at very steep angles towards the East. Vertical semi-brittle strike-slip shear zones trending in general N-S to NNE-SSW, i.e., parallel to the foliation diminish the strength of the rock mass.

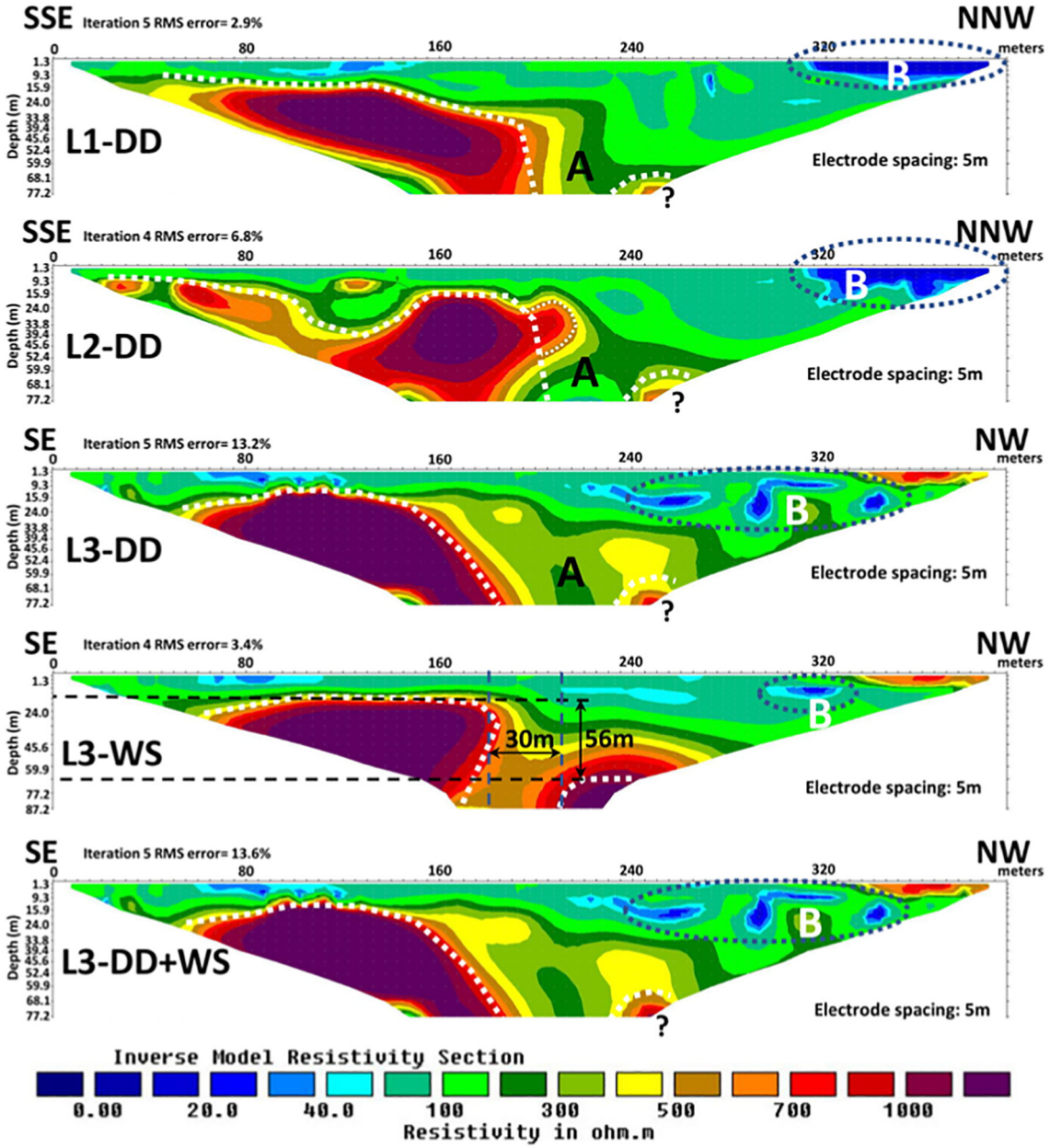

Fig. 8. Inverted resistivity sections along the three profiles shown in Figs. 2 and 6. The results for different acquisition electrode arrays (DD, WS and combined DD + WS) are also presented. White dotted lines depict the bedrock at the southern study area. Question mark symbol used to show the ambiguous interpretations.

Important structures, however, are the extensional faults dipping to the NE-ENE at medium to steep angles. Also, the fact that dikes with orientation similar to mapped Miocene gabbro dikes (Wier and Hadley, 1975; Hadley and Fleck, 1980) make the bedrock underneath the stream bed to present several anomalies as defined by the geophysical survey. In fact, geophysical results suggest two main anomalies (A and B) (Fig. 8). The first anomaly (A) is dipping vertically to near-vertically boundary, subdividing the ERT profiles in two parts: the first part is the southern half one which is characterized by 2 layer stratigraphy composed with overlying alluvium and the second part is the underlying bedrock that ranges in depth from 10 m to 30 m. This anomaly, taking into account the tectonic structures defined herein, is attributed to the intersection of the ENE-dipping normal faults with a possibly buried gabbro dike striking NW-SE, since the erosion of these dykes is much higher than the host rock, giving rise to the abrupt lowering of the bedrock relief beneath the alluvium. The second anomaly (B) is related to the existence of the most surficial layer that has been mainly observed in ERT L 1, L2 and partly L3. This anomaly is characterized by relatively very low resistivity (5–20 Ohm.m) and with abnormal boundaries within the first layer in L3. This anomaly can be interpreted as geothermal fluids. Particularly, this hot water path can be correlated with the intersection of the ENE-dipping normal faults with the shear and fault zones that align parallel to the main N-S to NNE-SSW fabric in the area (Fig. 11). Moreover, our results consistent with previous study (Mohamed et al., 2013), who concluded that almost all surface structural lineaments which control the movement of the geothermal water in the Ain Al Harrah hot spring, i.e., a hot spring only about 3 km southern the study site along the Al Lith Wadi, follow the main structural trends of Wadi Al-Lith area (Bibby et al., 1984).

TEM results provided supplementary information about the NW part of the study area, which was not accessible by the ERT method (due to lack of space for acquiring data). The first layer is characterized

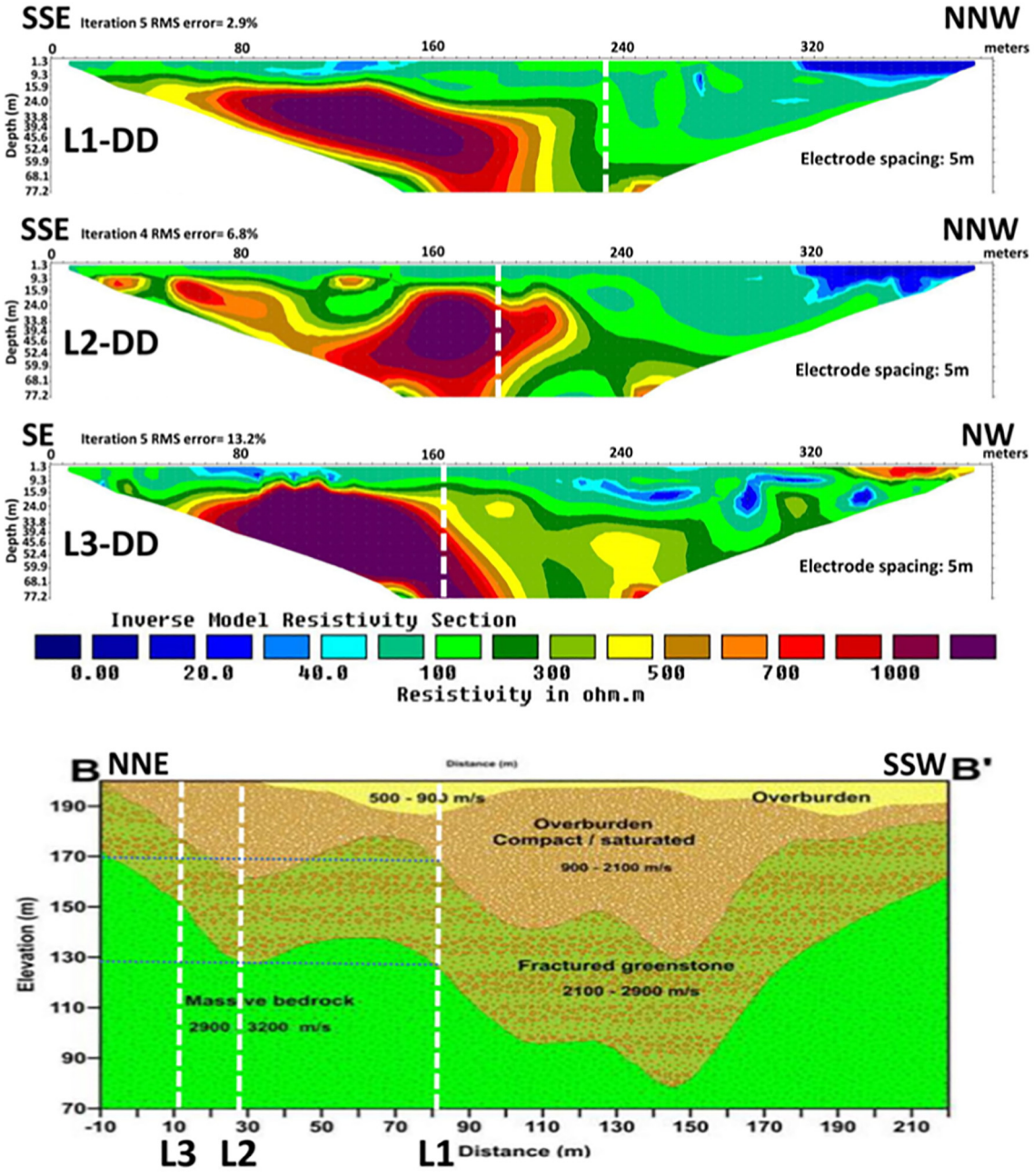

Fig. 9. Comparison of a refraction (B-B′) profiles from (Moustafa et al., 2013) with three ERT profiles acquired in this study.

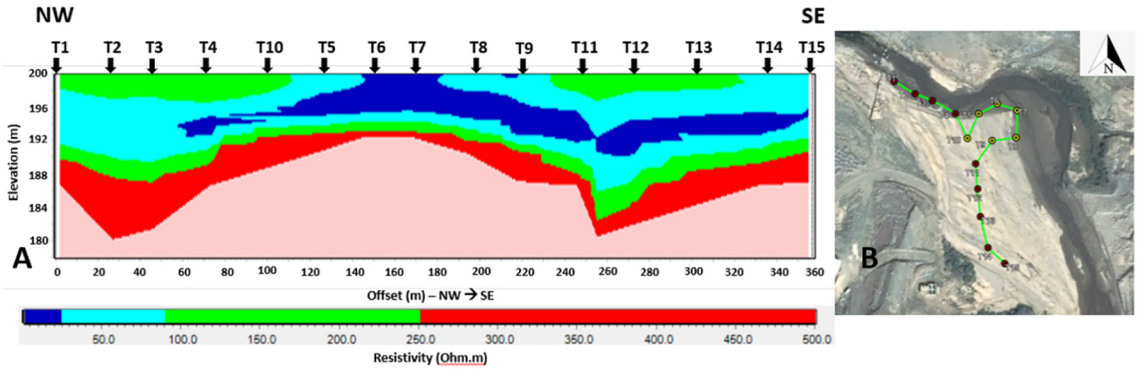

Fig. 10. A) The quasi-2D TEM resistivity section is presented. B) The location/geometry of the TEM soundings are shown.

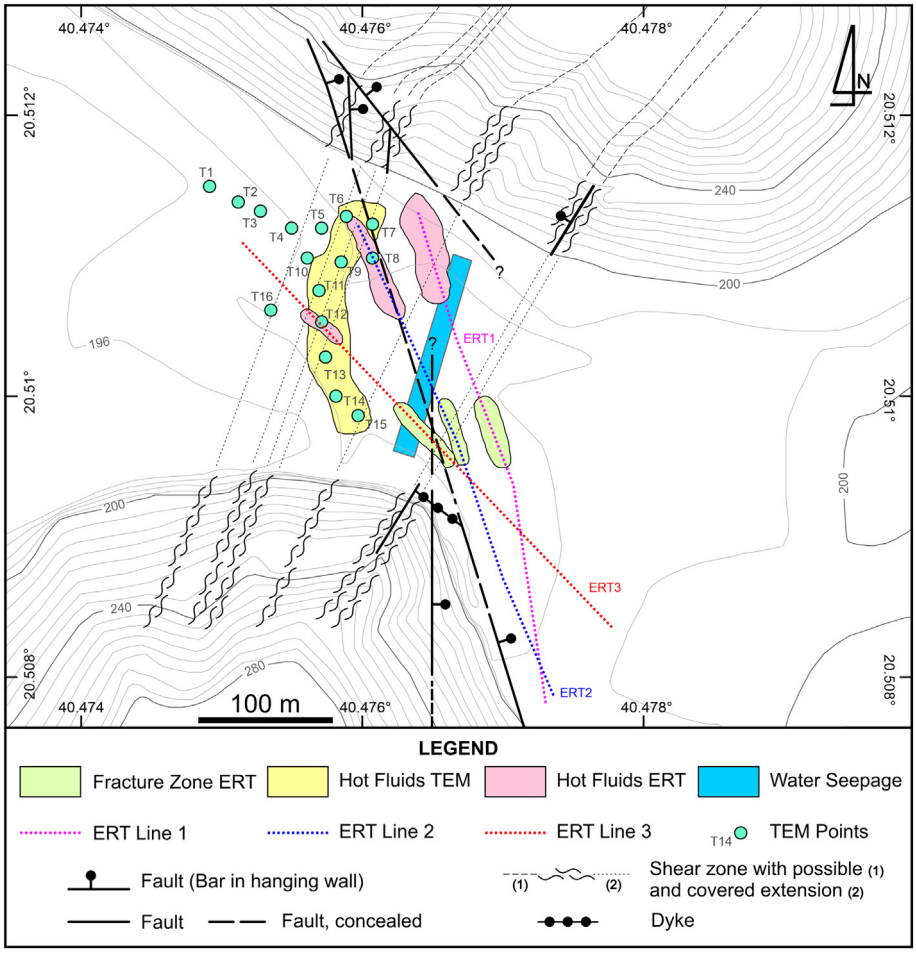

Fig. 11. Overall interpretation of the study area using both geological and geophysical investigations.

by resistivity values less than 20 Ohm.m (dark blue color), representing the presence of hot (geothermal) fluids which were detected by the ERT profiles and observed by the field crew during the electrical tomographic measurements. The saturated sediments are characterized by resistivity values varying from 20 to 90 Ohm.m (light blue color). The more compacted sediments (sand with gravels) or the fractured and saturated greenstone are correlated with higher resistivity values (90–250 Ohm.m, green color), while the bedrock of the study area is correlated with resistivity values higher than 250 Ohm.m. Based on the final quasi-2D resistivity section (Fig. 10), an uplift of the bedrock is found between soundings T5 to T9. The depth to the bedrock at these sites was almost 7 m below the ground surface. Two troughs were also found, beneath T2 and T3 soundings, where the depth to the bedrock is about 29 m below the ground surface, whereas the depth to the bedrock beneath T9 and T13 soundings is about 28 m below the ground surface. The very low resistivity zone is observed covering both sides of the uplift where it is mainly extended to the SE (blue shaded zone in Fig. 11), as is also shown in the quasi-2D resistivity section (Fig. 10). The integrated geological and geophysical results at the study site are shown in Fig. 11.

7. Conclusions and recommendations

Geological and geophysical investigations have been carried out at the Wadi Al Lith site to understand the local geological condition at the study site. The results delineate the tectonic features of the study site as well as the associated rock types. The exposed rocks types are mainly greenstones and greenschists metamorphosed from basalts, andesites and volcaniclastic rocks where these rocks are highly sheared and foliated, affecting their strengths (brittle rocks). The geophysical investigations reveal the presence of subsurface fracture and shear zones, faults, and geothermal hot fluids. Moreover, the geophysical studies show that the bedrock at the study site is found to be irregular where abrupt throw along the traverse of the wadi is observed. Hence, this study successfully delineates fractures/faults zones and hot water flow paths. It also shows that the study site has been subjected to many geological events such as faulting, shearing, foliation, and stretching. The delineated structures and the other geological elements are considered as weak zones from the geotechnical point of view and should be considered. The current study shows that an integrated/combined geophysical, geological, geotechnical engineering, and satellite investigations is needed, prior to any development construction, enhancing the construction safety and efficiency. Such integrated surveys are cost-effective and fast to be implemented and are highly recommended during an engineering site characterization before giving any approval for any development construction.

Declaration of Competing Interest

The authors declare that they have no known competing financial interests or personal relationships that could have appeared to influence the work reported in this paper.

References

Al-Homoud, Azm S., Taqieddin, Salah A., Ahmad, Fadhil H., 1995. Geologic problems related to dam sites in jordan and their solutions. Eng. Geol. 39 (3–4), 233–263.

Al-Sanad, H.A., Ismael, N.F., Nayfeh, A.J., 1993. Geotechnical properties of dune sands in Kuwait. Eng. Geol. 34 (1–2), 45–52.

Autio, U., Smirnov, M. Yu, Savvaidis, A., Soupios, P., Bastani, Mehrdad, 2016. Combining electromagnetic measurements in the mygdonian sedimentary Basin, Greece. J. Appl. Geophys. 135, 261–269.

Bibby, H.M., Dawson, G.B., Rayner, H.H., Stagpoole, V.M., Graham, D.J., 1984. The structure of the mokai geothermal field based on geophysical observations. J. Volcanol. Geotherm. Res. 20 (1–2), 1–20.

Brown, G.F., Jackson, R.O., Bogue, R.G., Maclean, W.H., 1963. Geologic map of the southern hijaz quadrangle, kingdom of Saudi Arabia: Us Geol. Surv. Misc. Geol. Inv. Map I-210A, Scale 1, 500000.

Brown, Glen F., 1970. Eastern margin of the red sea and the coastal structures in Saudi Arabia. Philosophical Transactions for the Royal Society of London. Series A, Mathematical and Physical Sciences, pp. 75–87.

Coleman, R.G., Donato, M.M., 1979. Oceanic plagiogranite revisited. Developments in Petrology. 6. Elsevier, pp. 149–168.

Coleman, R.G., Brown, G.F., Keith, T.E.C., 1972. Layered gabbros in Southwest Saudi Arabia. Prof. Pap. US Geol. Surv. 800, 143–150.

Coleman, Robert Griffin, 1974. Geologic background of the red sea. The Geology of Continental Margins. Springer, pp. 743–751.

Demirci, İsmail, Candansayar, Mehmet Emin, Vafidis, Antonis, Soupios, Pantelis, 2017. Two dimensional joint inversion of direct current resistivity, radio-magnetotelluric and seismic refraction data: An application from bafra plain, Turkey. J. Appl. Geophys. 139, 316–330.

Denmark Skolegade 21, 2020. 18000 Aarhus C. Aarhus Geosoftware.

Everett, Mark E., 2013. Near-Surface Applied Geophysics. Cambridge University Press.

Everett, Mark E., Meju, Max A., 2005. Near-surface controlled-source electromagnetic induction. Hydrogeophysics. Springer, pp. 157–183.

Fleck, Robert J., Greenwood, W.R., Hadley, D.G., Anderson, R.E., Schmidt, D.L., 1980. Rubidium-strontium geochronology and plate-tectonic evolution of the southern part of the arabian shield. Technical report, US Geological Survey; for sale by the Supt. of Docs., GPO.

Hadley, D.G., Fleck, R.J., 1980. Reconnaissance geologic map of the al lith quadrangle, sheet 20/40 c. Kingdom of Saudi Arabia: Saudi Arabian Directorate General of Mineral Resources Geologic Map GM-32, scale. 1, p. 10 (100,000).

Hadley, Donald G., Fleck, Robert Joseph, 1979. Reconnaissance geology of the al lith quadrangle, sheet 20/40 c, kingdom of Saudi Arabia. Technical Report, US Geological Survey.

Hoekstra, Pieter, Blohm, Mark W., 1990. Case histories of time-domain electromagnetic soundings in environmental geophysics. Geotechn. Environm. Geophys. 2, 1–15.

Kalisperi, Despina, Kouli, Maria, Vallianatos, Filippos, Soupios, Pantelis, Kershaw, Stephen, Lydakis-Simantiris, Nikos, 2018. A transient electromagnetic (tem) method survey in north-central coast of Crete, Greece: evidence of seawater intrusion. Geosciences 8 (4), 107.

Kanta, Asimina, Soupios, Pantelis, Barsukov, Pavel, Kouli, Maria, Vallianatos, Filippos, 2013. Aquifer characterization using shallow geophysics in the keritis basin of western Crete, Greece. Environ. Earth Sci. 70 (5), 2153–2165.

Kirsch, Reinhard, 2006. Groundwater Geophysics. 493. Springer.

Lashin, A., Chandrasekharam, D., Al Arifi, N., Al Bassam, A., Varun, C., 2014. Geothermal energy resources of Wadi al-lith, Saudi Arabia. J. Afr. Earth Sci. 97, 357–367.

Li, Ruiheng, Hu, Xiangyun, Xu, Dong, Yang, Liu, Nian, Yu., 2020. Characterizing the 3d hydrogeological structure of a debris landslide using the transient electromagnetic method. J. Appl. Geophys. 103991.

Loke, Meng Heng, 2004. Tutorial: 2d and 3d Electrical Imaging Surveys.

Loperte, A., Soldovieri, F., Palombo, A., Santini, F., Lapenna, V., 2016. An integrated geophysical approach for water infiltration detection and characterization at Monte cotugno rock-fill dam (southern Italy). Eng. Geol. 211, 162–170.

Mohamed, T., Hussein, Aref Lashin, Al Bassam, Abdulaziz, Al Arifi, Nassir, Al Zahrani, Ibrahim, 2013. Geothermal power potential at the western coastal part of Saudi Arabia. Renew. Sust. Energ. Rev. 26, 668–684.

Moisidi, M., Vallianatos, F., Soupios, P., Kershaw, S., Rust, Derek, Piscitelli, S., 2013. Modelling tectonic features of the kissamos and paleohora areas, western crete (Greece): combining geological and geophysical surveys. J. Geophys. Eng. 10 (2), 025015.

Moustafa, Sayed S.R., Ibrahim, Elkhedr H., Elawadi, Eslam, Metwaly, Mohamed, Al Agami, Naser, 2013. Seismic refraction and resistivity imaging for assessment of groundwater seepage under a dam site, Southwest of Saudi Arabia. Int. J. Phys. Sci. 7 (48), 6230–6239.

Nabighian, M.N., 1988. Electromagnetic Methods in Applied Geophysics, Volume 1–Theory. Tulsa, Society of Exploration Geophysicists.

NESPAK – National Engineering Services Limited Pakistan, 2014. Design review report of al lith dam, kingdom of Saudi Arabia. rev.3. p. 71 Unpublished results.

Ntarlagiannis, Dimitrios, Robinson, Judith, Soupios, Pantelis, Lee, Slater, 2016. Field-scale electrical geophysics over an olive oil mill waste deposition site: evaluating the information content of resistivity versus induced polarization (ip) images for delineating the spatial extent of organic contamination. J. Appl. Geophys. 135, 418–426.

Rahimi, Salman, Wood, Clinton M., Coker, Folaseye, Moody, Timothy, Bernhardt-Barry, Michelle, Kouchaki, Behdad Mofarraj, 2018. The combined use of masw and resistivity surveys for levee assessment: A case study of the melvin price reach of the wood river levee. Eng. Geol. 241, 11–24.

Rani, Payal, Soupios, Pantelis, Barsukov, Pavel, 2020. Regional tectonic model of southern, central part of the mygdonian basin (Northern Greece) by applying 3d transient electromagnetic modeling. J. Appl. Geophys. 104008.

Reynolds, John M., 2011. An Introduction to Applied and Environmental Geophysics. John Wiley & Sons.

Ross, David A., Schlee, John, 1973. Shallow structure and geologic development of the southern red sea. Geol. Soc. Am. Bull. 84 (12), 3827–3848.

Simyrdanis, Kleanthis, Papadopoulos, Nikos, Soupios, Pantelis, Kirkou, Stella, Tsourlos, Panagiotis, 2018. Characterization and monitoring of subsurface contamination from olive oil mills' waste waters using electrical resistivity tomography. Sci. Total Environ. 637, 991–1003.

Smith, Douglas L., Randazzo, Anthony F., 1986. Evaluation of electrical resistivity methods in the investigation of karstic features, el cajon dam site, honduras. Eng. Geol. 22 (3), 217–230.

Soupios, Pantelis M., Kalisperi, Despina, Kanta, Asimina, Kouli, Maria, Barsukov, Pavel, Vallianatos, Filippos, 2010. Coastal aquifer assessment based on geological and geophysical survey, Northwestern Crete, Greece. Environ. Earth Sci. 61 (1), 63–77.

Sudha, Kumari, Tezkan, Bülent, Israil, Mohammad, Rai, Jagdish, 2011. Combined electrical and electromagnetic imaging of hot fluids within fractured rock in rugged himalayan terrain. J. Appl. Geophys. 74 (4), 205–214.

Wang, Tao, Chen, Jiansheng, Li, Ping, Yin, Yajuan, Shen, Chengji, 2019. Natural tracing for concentrated leakage detection in a rockfill dam. Eng. Geol. 249, 1–12.

Wier, Kenneth Leland, Hadley, Donald G., 1975. Reconnaissance Geology of the Wadi Sa'diyah Quadrangle [20/40A]: U.S. Geological Survey Saudi Arabian. Project Report PR-193 p. 27.